Simulation of a supersonic hydrogen-air autoignition-stabilized flame using reduced chemistry

P. Boivin[a,*], A. Dauptain[c], C. Jiménez[a,b], B. Cuenot[c]

[a]*Dept. Ingeniería Térmica y de Fluidos, Universidad Carlos III de Madrid, Leganés 28911, Spain*
[b]*Centro de Investigaciones Energéticas, Medioambientales y Tecnológicas, Madrid, Spain*
[c]*Centre Européen de Recherche et de Formation Avancée en Calcul Scientifique, 42 ave. G. Coriolis 31 057 Toulouse Cedex 1, France*

Abstract

A three-step mechanism for H_2-air combustion (Boivin et al., Proc. Comb. Inst. 33, 2010) was recently designed to reproduce both autoignition and flame propagation, essential in lifted flame stabilization. To study the implications of the use of this reduced chemistry in the context of a turbulent flame simulation, this mechanism has been implemented in a compressible explicit code and applied to the simulation of a supersonic lifted co-flowing hydrogen-air flame. Results are compared with experimental measurements (Cheng et al. C&F 1994) and simulations using detailed chemistry, showing that the reduced chemistry is very accurate. A new explicit diagnostic to readily identify autoignition regions in the post-processing of a turbulent hydrogen flame simulation is also proposed, based on variables introduced in the development of the reduced chemical mechanism.

Keywords: Turbulent Autoignition, Hydrogen, Reduced Chemistry, Supersonic Flame

1. Introduction

With the democratization of high-performance technical computing, reliance on the numerical computation of combustion processes is growing. Ensuring the accuracy of the methods and models used in numerical simulation of combustion is therefore critical. One element in achieving this accuracy is to base the calculations on a correct detailed chemical-kinetic mechanism, but this usually leads to prohibitively expensive calculations. This has promoted numerous studies on chemistry reduction methods, among which hydrogen-oxidation has been a pioneer as relatively few elementary reactions and reactive species are involved (resp. 21 and 8), and the reaction rates are well validated under most conditions [1]. Accordingly, a number of explicit reduced mechanisms for hydrogen combustion have been proposed in the past [2–8], designed to reproduce accurately one combustion process in particular – autoignition, deflagrations, or diffusion flames – and for a limited range of temperature, pressure or equivalence ratios. In many practical applications, however, these combustion processes can be encountered simultaneously – and possibly under a wide range of conditions – which renders the use of such reduced chemistries inadequate.

A three-step mechanism for H_2-air combustion was recently proposed [9], designed to cope with high-temperature autoignition, diffusion flames and flame propagation. To encompass autoignition, a specific correction was included in the mechanism, based on an eigenvalue analysis of the chain-branching reactions between reactants and the main radicals. It has been validated in premixed and non-premixed laminar flames, as well as laminar autoignition, for a wide range of pressure, temperature and equivalence ratios.

The purpose of the present paper is twofold. The first objective is to complete the validation of this three-step chemistry, in the context of turbulent autoignition. To this end, a supersonic lifted co-flowing hydrogen-air diffusion flame stabilized by autoignition is chosen as test case. Given that the flame involves autoignition, diffusion and premixed combustion processes under intensely fluctuating flow conditions, it is a challenging test case for the three-step chemistry. This objective is tackled in the first two sections of the paper. Systematic post-processing of such unsteady three-dimensional lifted flame simulations to analyze stabilization is a challenge [10–15] because the instantaneous stabilization position typically fluctuates rapidly. Moreover non-premixed combustion, premixed combustion and autoignition processes can contribute simultaneously to stabilization. Fifteen years ago, the Takeno flame index was introduced to identify premixed and non-premixed combustion [10]. Identification of autoignition remains nowadays an active subject [11], as the role of autoignition in flame stabilization is still actively studied [13]. Being able to identify in a systematic manner zones where autoignition originates is a crucial issue. Section 4 presents a new explicit diagnostic to readily identify regions where autoignition is occurring, based on joint use of quantities inspired by [9, 11, 14]. The diagnostic is fully explicit, which makes it computationally cheap, and easily accessible both at the post-processing stage and in run-time.

*Corresponding author
Email address: pboivin@ing.uc3m.es (P. Boivin)

2. Description of the supersonic flame

The supersonic burner (SSB) of the NASA Langley Research Center [16] sketched in Fig. 1 and with operating conditions given in Table 1, produces an axy-symmetric flame from a sonic pure hydrogen cold jet surrounded by a largely supersonic (Mach 2) jet of hot products generated by a lean combustor. Massive convection leads to a large induction zone, preceding the flame stabilization area, about 6 cm from the nozzle exit, or 25 D (D=2.36 mm, is the diameter of the inner hydrogen jet). The work of Cheng et al. [16] with the SSB provides accurate experimental data on the dynamics, the mixing and the combustion conditions of this supersonic lifted flame. Through combining ultraviolet spontaneous vibrational Raman scattering and laser-induced predissociative fluorescence techniques, they obtained simultaneous instantaneous measurements for temperature and species concentrations (main species and OH radical). Measurements are reported as radial profiles at distances x/D = 0.85, 10.8, 21.5, 32.3, 43.1, 64.7 and 86.1 from the burner exit and as scatter plots of temperature and species at several selected locations.

2.1. Numerical set-up

Simulations of the supersonic flame described above are carried out with the Navier-Stokes equations solver AVBP [17], developed at Centre Européen de Recherche et de Formation Avancée en Calcul Scientifique (CERFACS). AVBP is an un-
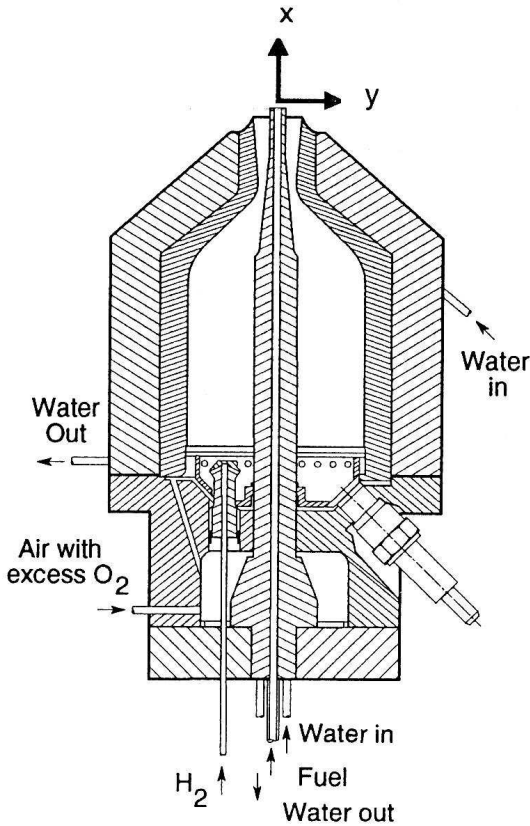
Dimensions	
Air mass flow rate (±2%)	0.0735 kg/s
H_2 mass flow rate (±2%)	0.000173 kg/s
O_2 mass flow rate (±3%)	0.0211 kg/s
fuel mass flow rate (±3%)	0.000362 kg/s
Nozzle exit inner diameter	17.78 mm
Fuel injector inner diameter	2.36 mm
Fuel injector outer diameter	3.81 mm
Vitiated Air Exit Conditions	
Pressure	107 kPa
Temperature	1250 K
Mach number	2.0
Velocity	1420 m/s
O_2 mole fraction	0.201
N_2 mole fraction	0.544
H_2O mole fraction	0.255
Fuel Exit Conditions	
Pressure	112 kPa
Temperature	540 K
Mach number	1.0
Velocity	1780 m/s
H_2 mole fraction	1.0

Table 1: Supersonic burner nominal operating conditions [16].

Figure 1: Sketch of the supersonic burner.

structured parallel compressible solver designed for Large Eddy Simulation (LES) or Direct Numerical Simulation (DNS) of combustion systems. The balance equations for mass, momentum, energy and species mass fractions are explicitly integrated with a 3rd-order scheme in space – Taylor Galerkin – and time – Runge-Kutta. To handle shocks in the supersonic jet the strategy proposed in [18] was followed: the sub-grid scale turbulent viscosity μ_t is modeled through a standard Smagorinsky model, a centered numerical scheme is chosen and a hyperviscosity like in [19] is used for capturing shocks. A subgrid scale diffusivity is introduced for chemical species via a turbulent Schmidt number equal to 0.6 (molecular diffusivity is different for each species, and specified by the Schmidt numbers : H_2: 0.28; O_2: 0.99; H_2O: 0.77; H: 0.17; O: 0.64; OH: 0.65; HO_2: 0.65; H_2O_2: 0.65; N_2: 0.87). No sub-grid turbulent combustion model is used, on the grounds that the resolved scales control fully the combustion processes in the region of interest for this study, that is, in the stabilization region. More details on this are given in the dimensional study in Sec. 2.3.
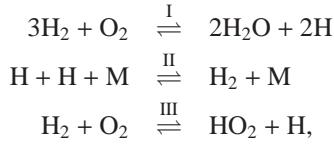
A number of groups have simulated the main characteristics of the supersonic flame using Eulerian and Lagrangian Monte Carlo Probability Density Function (PDF), or flamelet models [20–25], in a Reynolds Averaged Navier-Stokes (RANS) context. The boundary conditions have proven to be one of the most sensitive elements in simulating this flame. The experiments in [16] provide detailed data on the fluid mechanical scales and on the flow composition at x/D=0.85, a very short distance from the nozzle exit compared to the 25D experimental flame stabilization lift-off height. A set of velocity, temperature, pressure and main species concentrations profiles – consistent with the

experimental data and the nominal flow rates of the burner given in Tab. 1 – is imposed at the supersonic inlet of the simulation located at $x/D=0.85$. Homogeneous isotropic turbulence is then superimposed in the vitiated air coflow, with a rms velocity of 300 m/s, consistently with the 20% fluctuations in velocity at the jet exit reported in the experiment [16].

The computational domain is a hemisphere corresponding to $x \geq 0.85D$ and of radius 10000D, and the fully unstructured grid consists of 6.6M tetraedric cells, with a minimum volume of $\Delta v = 8.10^{-13}m^3$. The convex boundary on the sphere is an adiabatic wall, sufficiently far so that no wave reaches it during the simulation time.

2.2. Reaction mechanisms for hydrogen combustion

The main objective of this work is to test, in a turbulent case, the behavior of the recently published three-step mechanism for H_2-air combustion [9] by comparing it to a detailed chemical-kinetic mechanism [1], consisting of 21 elementary reversible reactions and involving 8 reacting species. The three-step mechanism was derived from a twelve-step skeletal mechanism by assuming O, OH, and H_2O_2 to be in chemical-kinetic steady state, and consists of three global reactions between five reacting species:

$$3H_2 + O_2 \overset{\text{I}}{\rightleftharpoons} 2H_2O + 2H$$
$$H + H + M \overset{\text{II}}{\rightleftharpoons} H_2 + M$$
$$H_2 + O_2 \overset{\text{III}}{\rightleftharpoons} HO_2 + H,$$

which rates ω_I, ω_{II} and ω_{III} are detailed in [9]. The three-step mechanism also includes a correction accounting for the failure of the steady state assumptions for O and OH during autoignition events above the second explosion limit, whose effectiveness and numerical stability has yet to be proven in a turbulent flame.

The correction consists in using modified rates $\omega_I^*/\omega_I = \omega_{II}^*/\omega_{II} = \omega_{III}^*/\omega_{III} = \Lambda$ during the chain-branching period that leads to autoignition. Λ, given in [9] depends on the local reactants concentrations and temperature.

It was shown in [14] that HO_2 is a good marker of autoignition. To identify when and where to use this correction, that is, when is autoignition occuring, a variable α was defined in [9] as

$$\alpha = \frac{\text{production rate}(HO_2) - \text{destruction rate}(HO_2)}{\text{production rate}(HO_2)}. \quad (1)$$

The occurrence of autoignition is identified by the condition that α be larger than a threshold value in regions of positive H-atom production. If this condition is not satisfied, the correction is not needed and $\Lambda = 1$ is to be used instead. The threshold criterion used in the computations was $\alpha > 0.05$, although the results were found to be quite independent of the threshold value used, provided the value selected was sufficiently small [9]. This switch could in principle cause numerical problems when autoignition occurs in a turbulent context, as strong gradients in reacting rates could be introduced. In order to understand the effect of the proposed correction, to study

the numerical stability of the switch, and to assess the accuracy of the three-step mechanism, the simulation of the supersonic flame was performed thrice, using the detailed San Diego chemistry, the reduced chemistry with the correction described above ($\omega_I^*/\omega_I = \omega_{II}^*/\omega_{II} = \omega_{III}^*/\omega_{III} = \Lambda$), and the reduced mechanism without the correction.

2.3. Physical scales and mesh requirements

The experiments show that the flame anchors in a flow of mean velocity $\overline{u} = 1200$m/s, which is hundreds of times the laminar flame speed of a hydrogen/air stoichiometric premixed flame. Even with a turbulence level of 20%, it is clear that the flame cannot be stabilized through a propagative edge flame, because the flow velocity is at least ten times higher than the deflagration speed. Instead, the flame of the present study is stabilized by the autoignition of a mixing layer between cold hydrogen and hot vitiated air.

The physical scales associated with the autoignition process are evaluated from a preliminary computation, in laminar conditions, in order to estimate the mesh resolution requirements in the turbulent computation. The transient evolution of a one-dimensional mixing layer of H_2 and vitiated air with composition and temperature as given in Tab.1 was computed using a DNS code with detailed chemistry and complex transport as in [26].
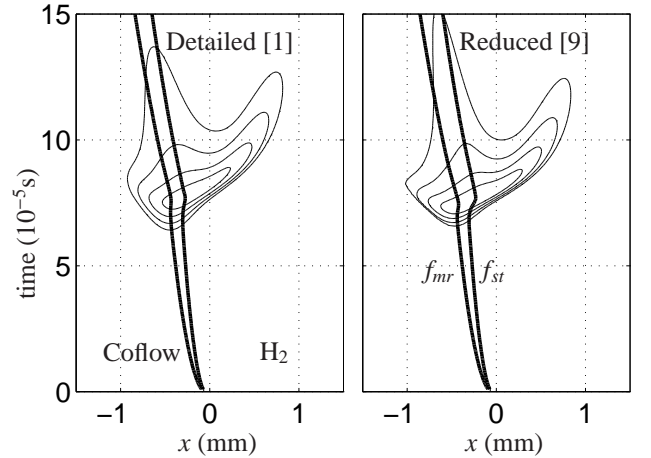
Figure 2: Isocontours of heat release rate corresponding to $2^n \times 10^9 J.m^{-3}.s^{-1}$ for $n = 1$ up to $n = 4$ in the transient one-dimensional mixing layer between the fuel and the vitiated air, with conditions given in Tab. 1. The black lines indicates the location where $f = f_{st}$ (stoichiometry) and $f = f_{mr}$ (most-reacting).

Autoignition occurs at the most-reacting mixture fraction f_{mr}, leading to the formation of two premixed fronts that leave behind a trailing diffusion flame [27]. The temporal triple-flame structure obtained using detailed and reduced chemistry is presented in Fig. 2. Also shown are lines corresponding to the evolution of the stoichiometric and most-reacting mixture fraction position (f_{st} and f_{mr}). The mixture fraction f is defined as

$$f = \frac{Z_H - Z_{H,coflow}}{Z_{H,fuel} - Z_{H,coflow}}. \tag{2}$$

Here, Z_H is the hydrogen elemental mass fraction in the mixture,

$$Z_H = \sum \mu_{i,H} Y_i, \tag{3}$$

where $\mu_{i,H}$ denotes the mass proportion of atomic hydrogen in the species i, and Y_i are their mass fractions. Figure 2 shows that autoignition occurs after a time $t_{ind.} \approx 6.10^{-5}$s, after which the flame ignites and splits into three branches : a lean, spatially decaying premixed flame (left branch), a diffusion flame anchored around the stoichiometry $f_{st}=0.03$ and a rich, spatially decaying premixed flame (right branch). The time scale associated with the premixed branches is denoted $t_{fl.}$ and estimated $\approx 4.10^{-5}$s.

Considering a mean velocity $\overline{u} = 1200$m/s estimated from the table of the fluid mechanical scales in the flame reported in [16], the induction zone should extend over a region of $t_{ind.}.\overline{u} \approx 30$D, and the premixed branches over $t_{fl.}.\overline{u} \approx 20$D in the laminar jet. In this stabilization region ($0 < x/$D < 50), mixing is a key phenomenon and must be captured from the largest to the smallest scales, i.e. in a DNS-like approach.

A very refined mesh was then used in the near burner area, $0.1 < \Delta x < 0.4$mm was imposed for $x/$D < 40, to ensure that mixing and ignition are well resolved, and there is no need for turbulent combustion modeling in this area. The ratio of the minimum grid spacing to the experimental integral and Kolmogorov scale are then respectively of the order of 0.02 and 10 according to the experiments by Cheng et al. [16]. A posteriori tests on the mesh resolution are presented in Appendix A.

Further downstream, the absence of a sub-grid turbulent combustion model will lead to an under-resolution of the diffusion flame. This does not imply numerical instabilities, as species and temperature gradients are controlled by the resolved flow. As the flame stabilization is the result of an autoignition process, and not an upstream propagation equilibrated by convection, the lack of subgrid model in the diffusion flame cannot affect the flame position.

The time step is limited by the smallest cell size and the fastest acoustic propagation speed $u + c$, u being the flow velocity, and c the sound speed, using a Courant-Friedrichs-Lewy criterion of 0.7. The resulting time-step is close to 2.10^{-8}s, which is at all times below any chemical-kinetic time scale.

3. Results

Computations were performed on a HP AMD cluster with 20.3 peak Tflops/s at CERFACS, using up to 120 cores.

3.1. Qualitative results

Figures 3 and 4 present the instantaneous and mean temperature and HO$_2$ mass fraction fields obtained in the simulation of the supersonic flame, and allow a first qualitative comparison between the three chemical-kinetic mechanisms. The highly fluctuating nature of the flame can be observed on the left side plots in Fig. 3, showing the instantaneous temperature field.

The left side plots in Fig. 4 show that HO$_2$ appears well before the high temperature region, indicating that autoignition is starting at distances of about 20D from the burner exit.
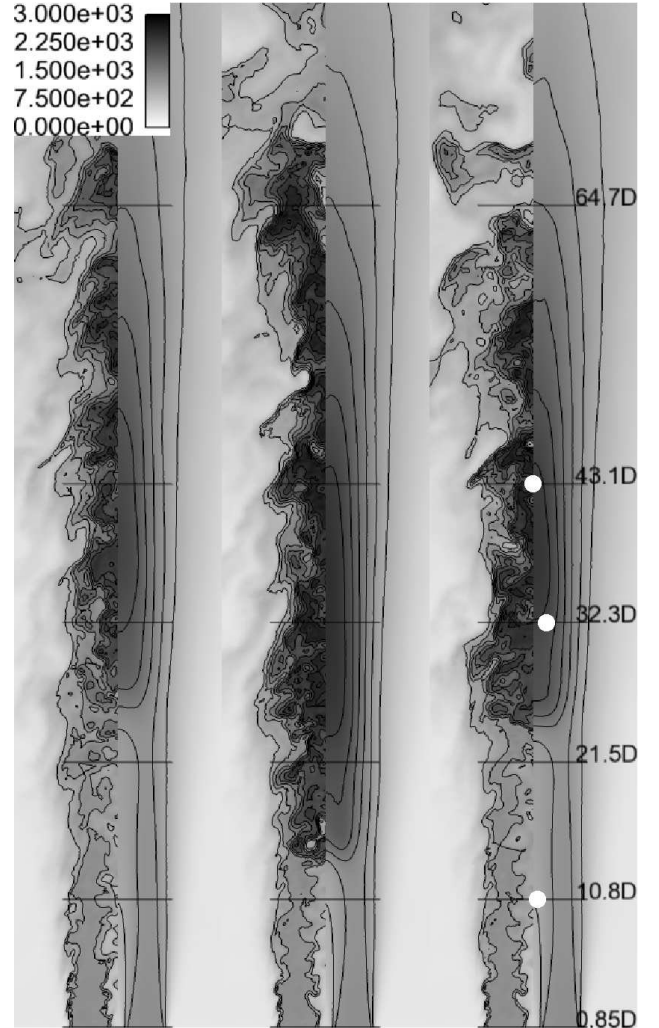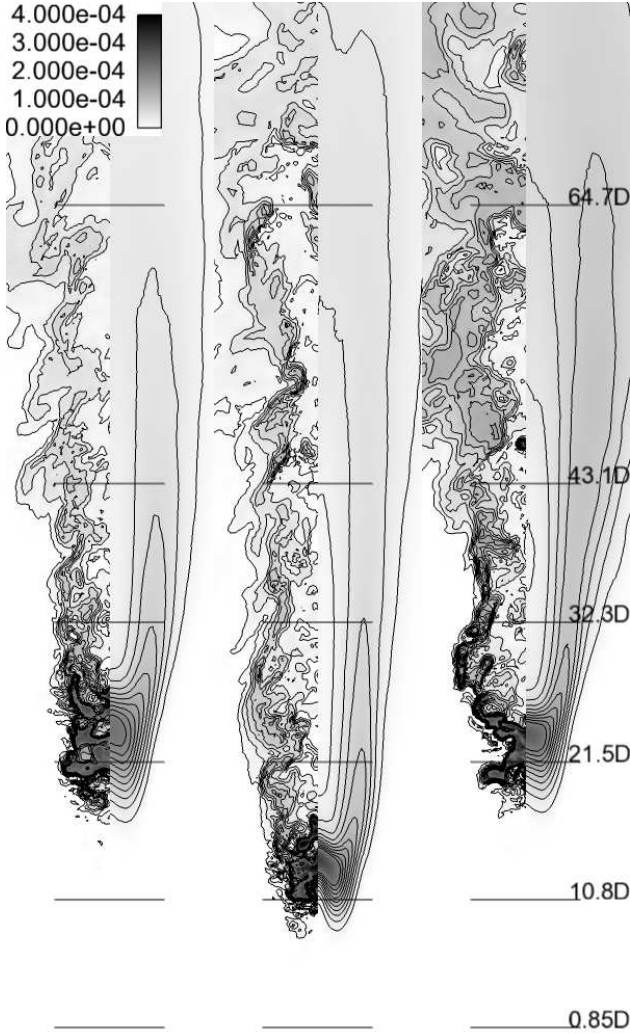

Figure 3: Instantaneous (left side) and mean (right side) temperature in the center plane of the flame. From left to right : detailed chemistry [1], reduced chemistry without the correction, and reduced chemistry as in [9]. Contour lines are plotted every 250K from 1000K to 2500K. White dots in the right plot correspond to the location of scatter plots of Figs. 7 to 9.

Focusing on the mean temperature in Fig. 3, the first noteworthy result is that the detailed chemistry predicts with good accuracy the stabilization position of the flame at about 25D from the supersonic burner, as obtained in the experiment, validating the choice of the San Diego detailed chemistry [1] as a reference. Secondly, the reduced mechanism including the adequate modified rates (ω_I^*, ω_{II}^* and ω_{III}^*) as presented in Sec. 2.2 predicts a very similar turbulent flame: the stabilization position, and the instantaneous and mean temperature and HO$_2$ radical mass fraction fields are very similar to those obtained with detailed chemistry.

Finally, the reduced mechanism without correction (middle

pictures in Figs. 3 and 4) expectedly results in a large underprediction of the stabilization height, about 40% shorter. Besides, the shape of the mean flame base indicates that this mechanism predicts a leaner autoignition, which is consistent with the laminar results presented in [9]. The inclusion of the correction of the reaction rates in the reduced chemistry changes drastically the stabilized flame, both in position and shape, indicating again that autoignition is the key mechanism in this flame stabilization.

Figure 4: Instantaneous (left side) and mean (right side) HO_2 mass fraction in the center plane of the flame. From left to right : detailed chemistry [1], reduced chemistry without the correction, and reduced chemistry as in [9]. Contour lines are plotted every 10^{-5} from 2.10^{-5} to 2.10^{-4}.

3.2. Comparison with experiment

A quantitative comparison of the flames obtained in the three simulations is presented in Fig. 5. It represents profiles for mean values and rms fluctuations of the temperature, mole fractions of main species H_2, O_2, H_2O, and radical HO_2 mole fraction along the flame axis, as obtained with the detailed chemistry, the reduced chemistry, and the reduced chemistry without

correction. Some experimentally measured points, extracted from radial profiles, are also included. They were obtained by interpolating at $y=0$ the radial profiles reported in [16]. Because of the asymmetry of the experimental radial profiles (Fig. 6), this interpolation does not necessarily correspond to the axis of the flame. The SSB, depicted in Fig. 1, shows a short combustion chamber fueled asymetrically by the hydrogen and oxygen injectors, followed by a short convergent divergent nozzle. The resulting flow is expected to be more asymmetric than the present CFD inlet conditions, which explains the deviation of the numerical results and experiments in these plots. As will be seen below, numerical and experimental radial profiles show a much better agreement.

Table 2 shows the lift-off height in D units, computed as the position of the maximum temperature gradient of the three mean temperature profiles in Fig. 5. These values confirm that the reduced mechanism without correction predicts the lift-off height with an error of more than 40%, while the introduction of the correction reduces the error to about 5%. In the remainder of the discussion, only the detailed mechanism and the reduced mechanism including the adequate correction will be considered.

	Lift-off height	Relative error
Detailed chemistry	26.12	0
Reduced chemistry	24.73	-5.35%
No correction	14.55	-44.5%

Table 2: Stabilization position in D units, as obtained with the detailed chemistry[1], the reduced mechanism [9], and the reduced mechanism without the correction. Experiments measure stabilization at 25D.

The reduced chemistry reproduces with good accuracy the mean and rms fluctuations profiles of all species predicted by the detailed chemistry. This is even true for the hydroperoxyl radical HO_2 (bottom plots in Fig. 5), which shows outstanding agreement in the induction zone, up to about x/D=20.

Figure 6 includes experimental and numerical radial profiles for mean values and rms fluctuations of the temperature, mole fractions of main species H_2, O_2, H_2O and radical HO_2 mole fraction at axial distances x/D=10.8, 21.5, 32.3 and 43.1. These axial locations are indicated in Figs. 3 and 4 for reference. Profiles at x/D=0.85 reported in the experiment are not included here, as this position corresponds to the inlet of the computational domain, where experimental profiles are directly imposed.

Mean and rms profiles in the induction zone, corresponding to positions x/D =10.8 and 21.5, and represented in Figs. 6.a and 6.b, are identical for the main species and temperature with the detailed and the reduced chemistry. They are also very similar for HO_2 mole fraction. Moreover, the agreement with the experimental mean values is very reasonable. Rms fluctuations in the simulation are comparable in magnitude to the experimental measurements, even if the central area peaks are not well reproduced.

Figures 6.c and 6.d show radial profiles for the same quantities at x/D=32.3 and 43.1, inside the stabilized flame. Mean values of the main species are still in good agreement for the detailed and the reduced mechanism, with small overestimations of HO_2 mass fraction in the diffusion flame. The two peaks observed in the numerical rms profiles in Figs 6.a and 6.b slowly merge into one as distance from the nozzle increases, giving a better agreement with the experiment.
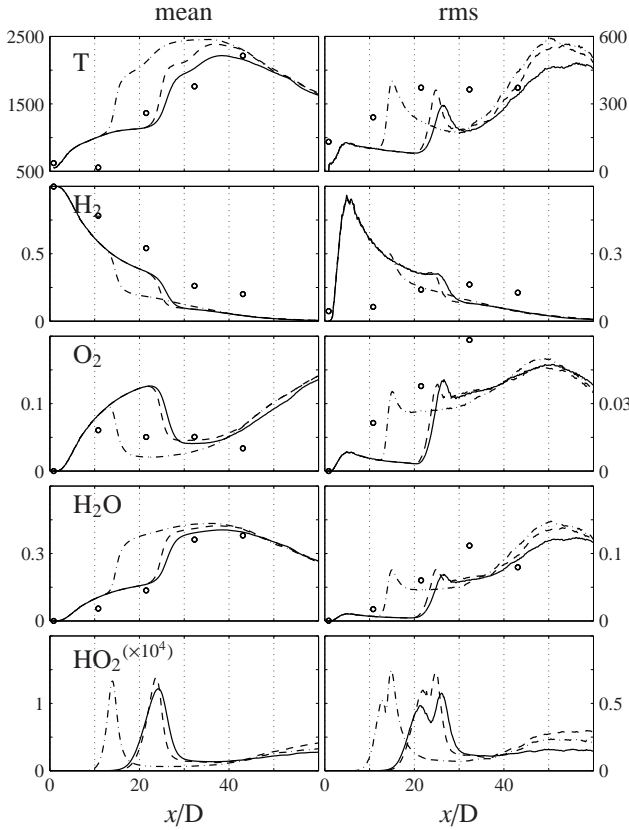

Figure 5: Mean and rms profiles for the temperature and mole fractions of selected species along the flame axis, as obtained with the detailed chemistry [1] (solid curves), with the reduced mechanism [9] (dashed curves), with the reduced mechanism without correction (dot-dashed curves), and in the experiments [16] (circles).

To further compare the numerical results and the experiments, scatter plots of temperature and species mole fractions are presented in Figs. 7 to 9. The left plots correspond to simultaneous experimental measurements at three locations [x/D, y/D]=[10.8, -0.65], [32.3, 1.1] and [43.1, 0] and the right plots to instantaneous values from the simulation with the reduced chemistry over 0.6ms at the same locations. The plots also show lines, representing the limits of pure mixing between the reactant streams (mixing line), and of adiabatic equilibrium after combustion (equilibrium line). Stoichiometry corresponds to $f_{st} = 0.03$.

The first scatter plots, in Fig. 7, correspond to the probe located at x/D = 10.8 and y/D = -0.65, in the induction zone, far from the ignition region (see Fig. 3). As expected, the temperature and main species are all very close to the mixing line, indicating that no reaction has occurred yet. This good agreement
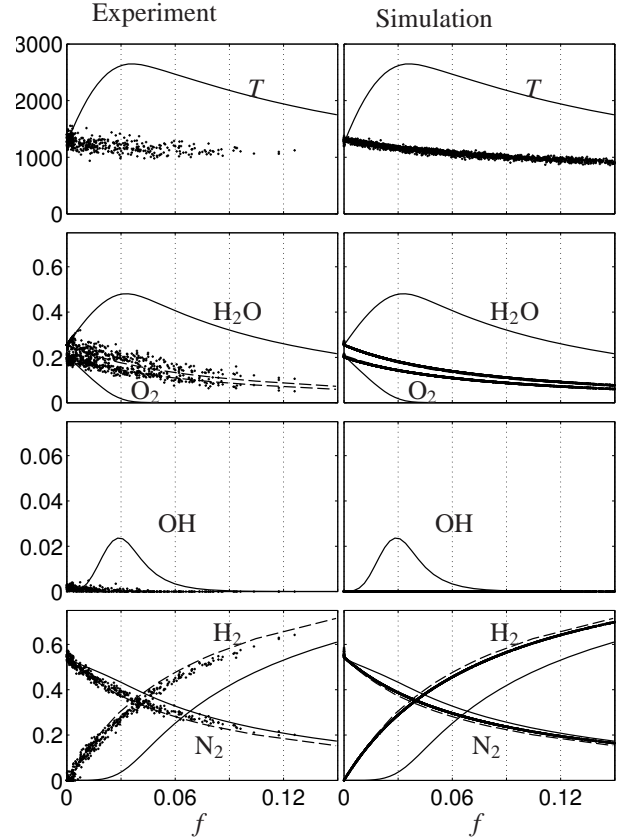

Figure 7: Scatter plots of temperature, main species mole fractions (H_2, O_2, N_2, H_2O), and OH mole fraction versus mixture fraction at x/D = 10.8, y/D= -0.65. Equilibrium (solid curve) and mixing lines (dashed curve) are also included. Left: Experiment. Right: Simulation.

validates the resolution of mixing at large scales, a sine qua non condition for the good prediction of the lift-off height. Some traces of OH, appear in the experiment at very low mixture fractions, which correspond to products of a lean pre-combustion in the SSB, as reported in the experiment [16], and not to the onset of ignition.

For the next scatter plots, in Figs. 8 and 9, probes are located inside the stabilized flame (see Fig. 3). The species and temperature progressively approach their adiabatic equilibrium level. The range of mixture fractions encountered at the second probe in Fig. 8, located in the flame, is fairly similar in the experiment and in the simulation ($f \in [0, 0.08]$ and [0,0.07] respectively). Agreement in the range of fluctuating f values is not as good at the last probe (Fig. 9), but remains acceptable.

Conditional averaging of the experimental and simulation scatter plots would show a good agreement, however, the scattering of the points in the vertical direction of these plots is noticeably different, as shown in Figs. 8 and 9. It is to be related to the lower rms fluctuations for temperature and species in the vicinity of the symmetry axis, as reported in Figs. 5 and 6.

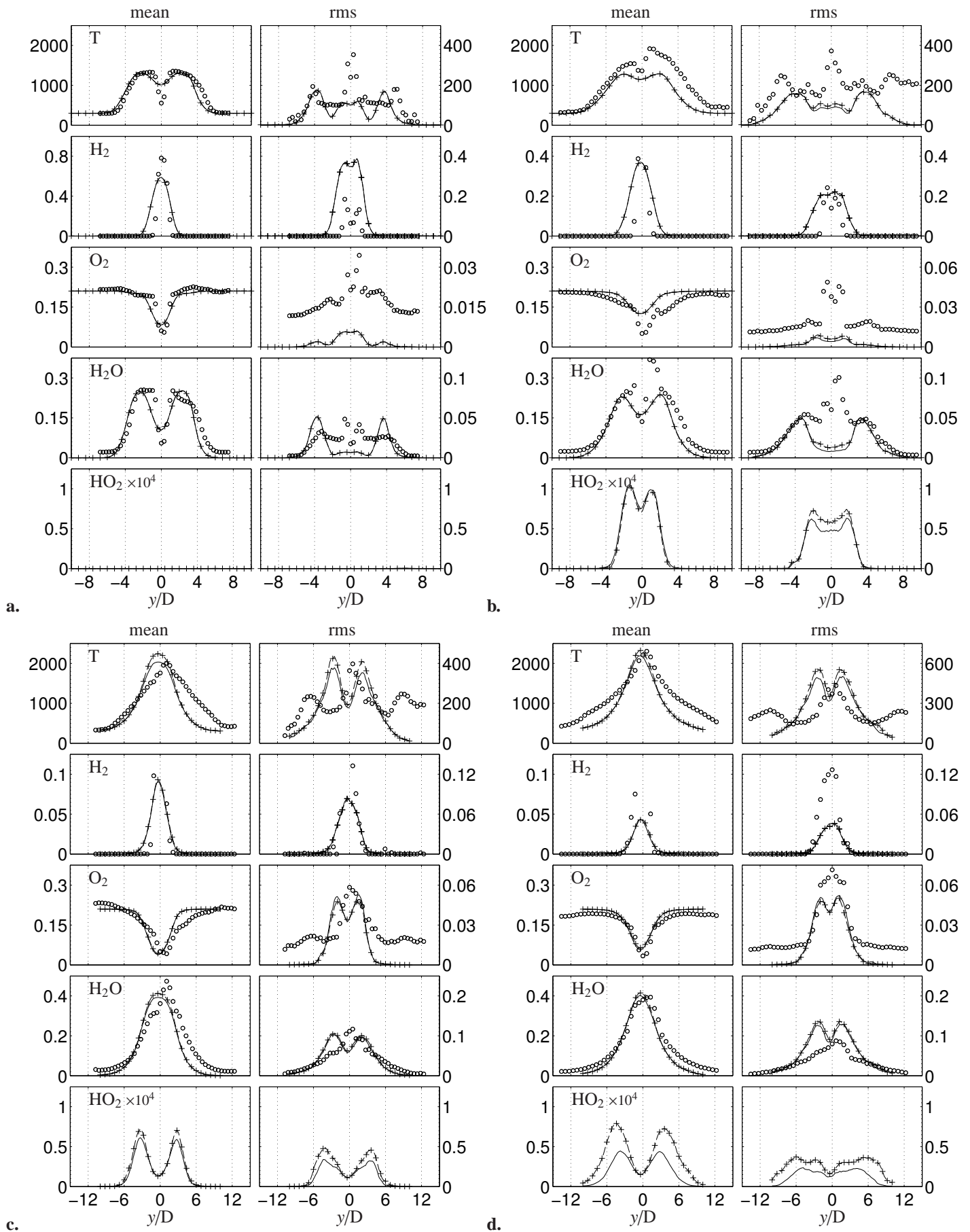This is due to the choice of the injected turbulence (homoge-

Figure 6: Mean and rms profiles for the temperature and mole fractions of selected species at (a) x/D=10.8, (b) 21.5, (c) x/D=32.3 and (d) 43.1, as obtained with the detailed chemistry [1] (solid curves), with the reduced mechanism [9] (dashed curves and crosses), and in the experiments [16] (circles).

7

neous isotropic), which does not describe the inhomogeneities produced by the splitter between the two jets. As a consequence, less fluctuations are found in this area compared to the experiment. This however seems to have a negligible impact on the global mixing (see Fig. 7). The quality of the simulated flow is then considered sufficient to study the impact of the finite-rate chemistry on flame stabilization.
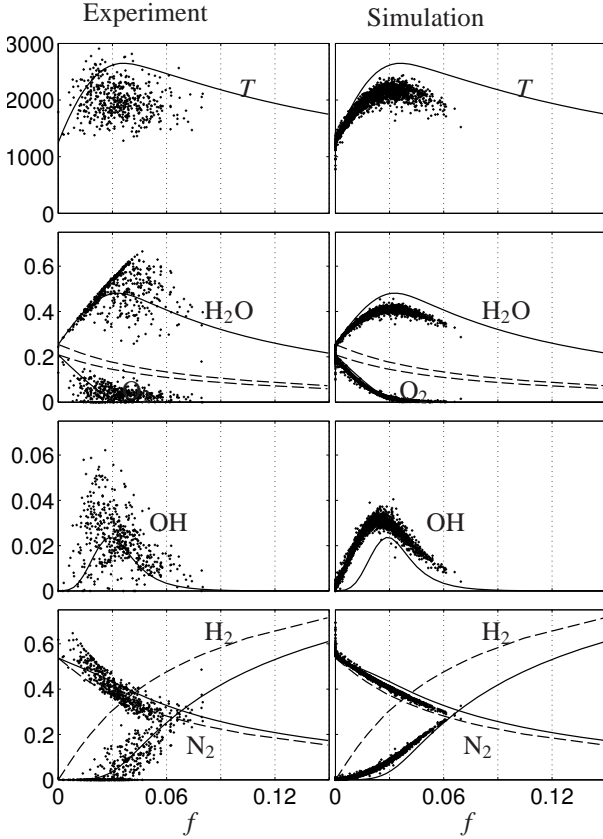

Figure 8: Scatter plots of temperature, main species mole fractions (H_2, O_2, N_2, H_2O), and OH mole fraction versus mixture fraction at $x/D = 32.3$, $y/D = 1.1$. Equilibrium (solid curve) and mixing lines (dashed curve) are also included. Left: Experiment. Right: Simulation.

We compare in Fig. 10 scatter plots of HO_2 mole fraction at $x/D=20$, $y/D=0$, (where instantaneous autoignition seems to start according to Figs. 3 and 4) as obtained with the detailed and the reduced chemistry. This area preceding the stabilization point contains the most important variations for the hydroperoxyl radical, while all other quantities remain close to the mixing line, indicating the onset of autoignition close to the most-reacting mixture fraction $f \approx f_{mr} = 0.015$. The similarity between the detailed and reduced chemistries indicate that the latter captures the main autoignition mechanism.

Figure 11 includes the same comparison for the temperature and the mole fractions of H_2, H_2O and OH in the mixture fraction space at $[x/D, y/D]=[25, 0]$. At this position, autoignition has occurred, and all species show intense fluctuations. Most of the hydroperoxyl has been consumed, triggering the chain-branching reactions characteristic of H_2 oxidation under these conditions.
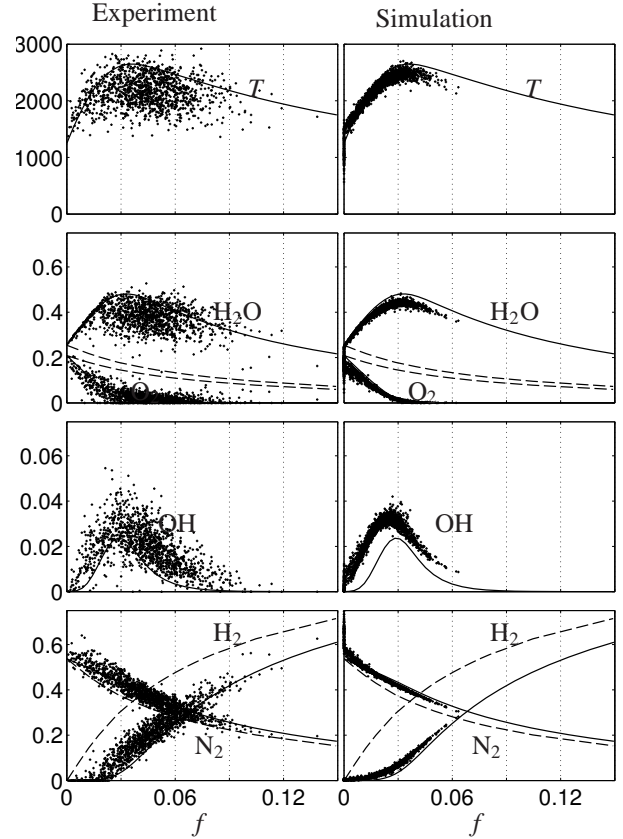

Figure 9: Scatter plots of temperature, main species mole fractions (H_2, O_2, N_2, H_2O), and OH mole fraction versus mixture fraction at $x/D = 43.1$, $y/D= 0$. Equilibrium (solid curve) and mixing lines (dashed curve) are also included. Left: Experiment. Right: Simulation.

In Fig. 11, OH radical, absent from the reduced chemistry, was estimated using the appropriate steady state expression given in [9], showing a reasonable agreement with the detailed chemistry.

3.3. Discussion

The comparison of the shapes of the mean and rms profiles in the induction zone preceding the flame, shown in Figs. 5, 6.a and 6.b. indicates that the mixing layer between hydrogen and the hot coflow is not well reproduced in the simulation. A better strategy for the inlet boundary condition should be investigated, to account for the non-uniformity of the turbulence at $x/D=0.85$, and the species fluctuations due to the unsteadiness of the flow characteristics after the pre-combustion chamber. However, this does not influence the flame stabilization, which seems to be purely chemistry related.

A second difference is that the experimental flame seems generally wider than the simulated flame. This error is recurrent in all recent simulations of this flame [20–25], and may be lessened by a more realistic boundary condition including, for instance, a realistic burner geometry.
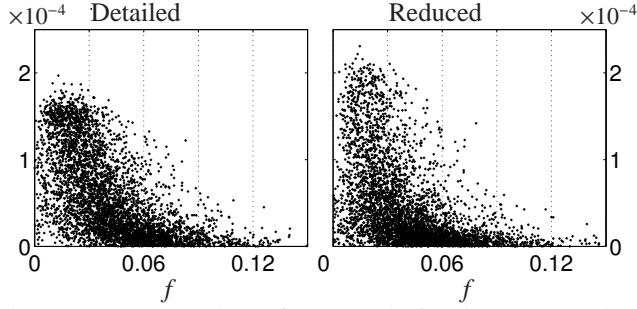
Figure 10: Scatter plots of HO_2 mole fraction versus mixture fraction at $x/D = 20$, $y/D = 0$. Left: detailed chemistry. Right: reduced chemistry.

Besides these inaccuracies, this flame simulation captures the correct physics, and is a good reference for studying the impact of the chemistry model, which is the objective of the present work.

The detailed and reduced chemistries predict mean values and rms fluctuations very similar for all main species, except in a very small area around 25D, as revealed in Fig. 11. This probe was purposely located in the area between the two stabilization positions predicted by the detailed and the reduced chemistries (resp. at about 26D and 24.5D, as presented in Tab. 2), to evaluate the size of the largest possible errors.

However, the burnt gases maximum temperature is overestimated by about 150K, as shown in Figs. 5, 6.c and 6.d. This is a well-known drawback of using explicitly reduced chemical mechanisms: the selected subset of radicals has a strong impact in the evaluation of the specific-heat C_p, and thus on thermodynamics.

4. An explicit diagnostic for autoignition identification.

The hydroperoxyl radical HO_2 peaks typically in igniting mixtures, therefore it has been extensively used for detection and visualization of autoignition in lifted-flames [13, 14, 28]. However, HO_2 concentration also peaks in ignited mixtures near the fuel-rich reaction zones of flames [11]. Moreover, its concentration during autoignition processes changes drastically with local conditions, and can hinder the detection of certain autoignition spots when several local maxima (in HO_2 level) are simultaneously present.

This section shows a possible use of the quantities derived in [9] and reviewed in Sec. 2.2 for a new explicit diagnostic to identify autoignition at the post-processing stage.

4.1. Reactivity of the mixture

The chemical explosive mode analysis (CEMA) proposed by Lu et al. [11, 29], and derived from the computational singular perturbation (CSP) method [30], is a method to quantify the reactivity of the mixture at each point of a simulation. Chemical explosive modes are associated with positive eigenvalues of the Jacobian of the chemical source term. In [11], explosive modes are detected by computing numerically the eigenvalues of the full Jacobian at every point of the computational domain. Here
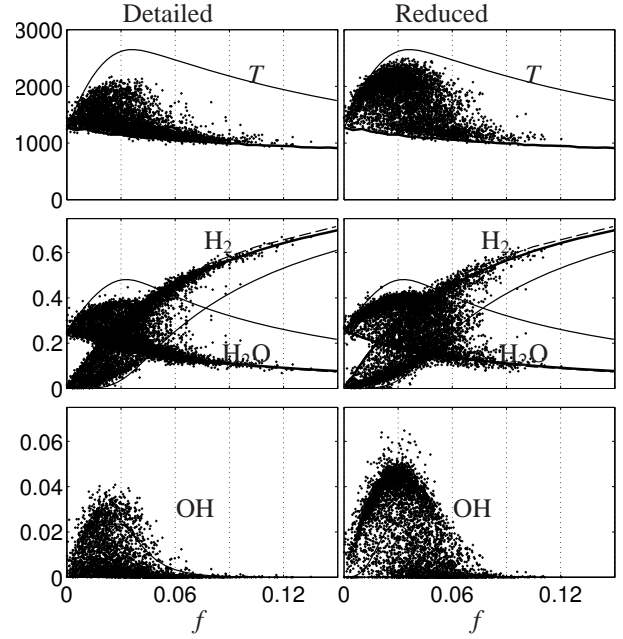

Figure 11: Scatter plots of temperature and selected species mole fractions (H_2, H_2O and OH) versus mixture fraction as obtained with detailed and reduced chemistry, at $x/D = 25$, $y/D = 0$. Equilibrium (solid curve) and mixing lines (dashed curve) are also included. Left: detailed chemistry. Right: reduced chemistry.

we propose an explicit expression for the eigenvalue associated to autoignition chemistry.
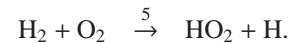
Hydrogen autoignition above the 2nd explosion limit can be characterized by the competition of the chain-branching reactions

$$O_2 + H \quad \overset{1}{\to} \quad OH + O$$
$$H_2 + O \quad \overset{2}{\to} \quad OH + H$$
$$H_2 + OH \quad \overset{3}{\to} \quad H_2O + H,$$
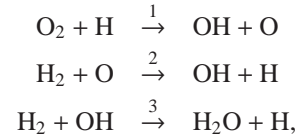
and the radical consumption through the third-body elementary reaction

$$H + O_2 + M \quad \overset{4}{\to} \quad HO_2 + M.$$
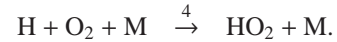
This competition can only occur if traces of radical are produced by the initiation step

$$H_2 + O_2 \quad \overset{5}{\to} \quad HO_2 + H.$$

Autoignition above the 2nd explosion limit can then be studied as the following linear system

$$\frac{d}{dt}\bar{C} = \mathbf{A}.\bar{C} + \bar{\epsilon}, \qquad (4)$$

where

$$\mathbf{A} = \begin{bmatrix} -(k_{1f} + k_{4f}C_M)C_{O_2} & k_{2f}C_{H_2} & k_{3f}C_{H_2} \\ k_{1f}C_{O_2} & -k_{2f}C_{H_2} & 0 \\ k_{1f}C_{O_2} & k_{2f}C_{H_2} & -k_{3f}C_{H_2} \end{bmatrix},$$

9

$$\bar{C} = \begin{bmatrix} C_H \\ C_O \\ C_{OH} \end{bmatrix} \quad \text{and} \quad \bar{\epsilon} = k_5 C_{O_2} C_{H_2} \begin{bmatrix} 1 \\ 0 \\ 0 \end{bmatrix}$$

Here the C_X are the molar concentrations of the species X, and $k_{if,i=1,5}$ are the forward temperature-dependent Arrhenius rates of the reactions listed above.

It can be shown that **A** has a single positive eigenvalue λ, characteristic of the chain-branching, which can be obtained with good approximation neglecting the cubic term in the characteristic polynomial [9], as:

$$\lambda = \frac{\sqrt{l_1^2 + 4l_0 l_2} - l_1}{2l_2}, \tag{5}$$

where the l_i are the coefficients of the characteristic polynomial:

$$l_2 = k_1 C_{O_2} + k_2 C_{H_2} + k_3 C_{H_2} + k_4 C_{O_2} C_M$$
$$l_1 = k_2 k_3 C_{H_2}^2 + (k_2 + k_3) k_4 C_{H_2} C_{O_2} C_M$$
$$l_0 = (2k_1 C_{O_2} - k_4 C_{O_2} C_M) k_2 k_3 C_{H_2}^2.$$

This simple expression for λ, depending only on the local reactant concentrations and temperature, gives an accurate estimation of the local non-premixed potential reactivity. It can also be used to estimate a priori the most-reacting mixture fraction f_{mr} [13, 26, 27], which corresponds to the maximum value of λ in a mixture.

Note that λ is proportional to the inverse of the autoignition time in homogeneous conditions. It is possible to obtain explicitly the relation between λ and the autoignition time, by fully integrating the differential equations (4), as in [31]. The complete integration results in an additional logarithmic term (associated to the initiation term $\bar{\epsilon}$), which was not found to improve significantly the identification of the most-reacting mixtures in this case.

Figure 12 presents a snapshot of the instantaneous λ value in the supersonic flame simulated in this work. Given that λ depends only on the local temperature and concentrations C_{H_2} and C_{O_2}, and because these quantities barely change during induction, λ is approximately constant along the most-reacting mixture line, marking reactivity but not the actual occurrence of ignition. Autoignition occurs along this line after sufficient accumulation of HO$_2$ radical, which can be identified by a second variable, as presented in next section.

4.2. Autoignition progress

Figure 13 shows the evolution of λ, the temperature and selected species mole fractions in an isobaric homogeneous reactor with initial conditions close to those encountered in the induction zone of the supersonic flame (p=1atm., T=1200K, f=0.03). It shows that, as explained above, the concentration of H$_2$, O$_2$, H$_2$O, H, as well as the temperature and therefore the reactivity λ remain constant during the induction process.

The chemical steady-state parameter α, defined in Eq. (1), was originally introduced in [14], and used later in [9] to detect autoignition and activate the correction in the 3-step reduced mechanism. The evolution of α during autoignition in the homogeneous reactor is included in the lower plot of Fig. 13. In
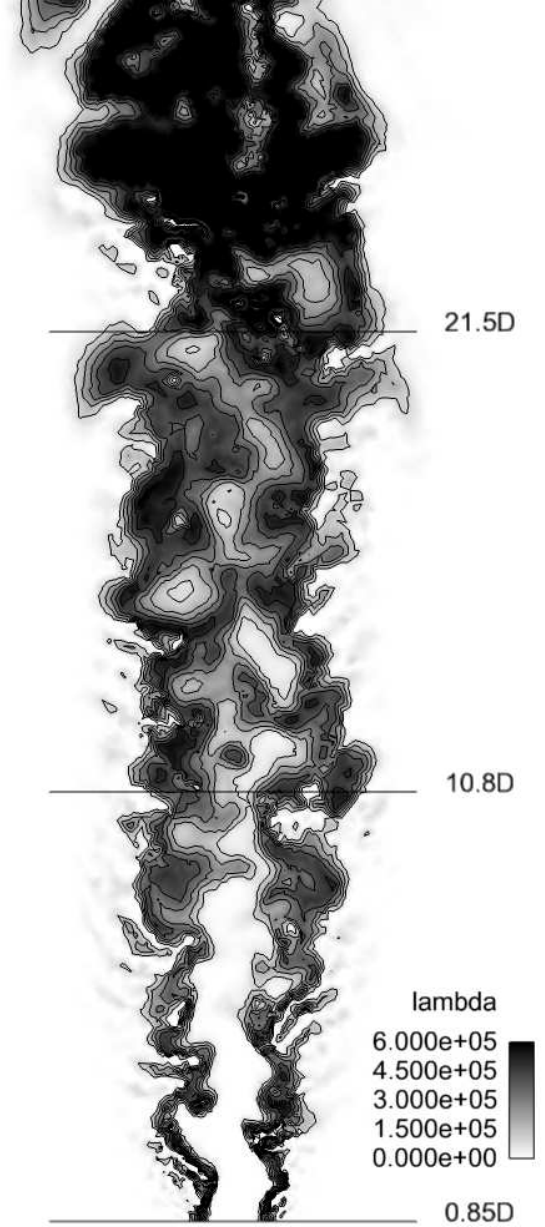

Figure 12: Snapshot of λ, the reactivity of the mixture. Contour lines at $\lambda = k.10^5 \text{s}^{-1}$, k=1,2,..,5.

the homogeneous autoignition process, HO$_2$ production starts by the initiation step H$_2$ + O$_2$ $\rightarrow$ HO$_2$ + H. While the produced H radical is readily consumed by the third-body reaction H + O$_2$ + M $\rightarrow$ HO$_2$ + M, producing more HO$_2$, HO$_2$ cannot be consumed by any of the reactants and α remains by definition unity during this stage. As HO$_2$ radical accumulates, α decreases, reaching 0 when the HO$_2$ concentration reaches its maximum value, triggering the autoignition. We can identify the autoignition period as the period when HO$_2$ progresses towards steady state, when α decreases. In Fig. 13 two vertical lines are plotted at $\alpha_{max} = 0.95$ and $\alpha_{min} = 0.05$ to show that these two values can be chosen as delimiters of the autoignition region. Given the variations of α (see Fig.13), the criterion de-
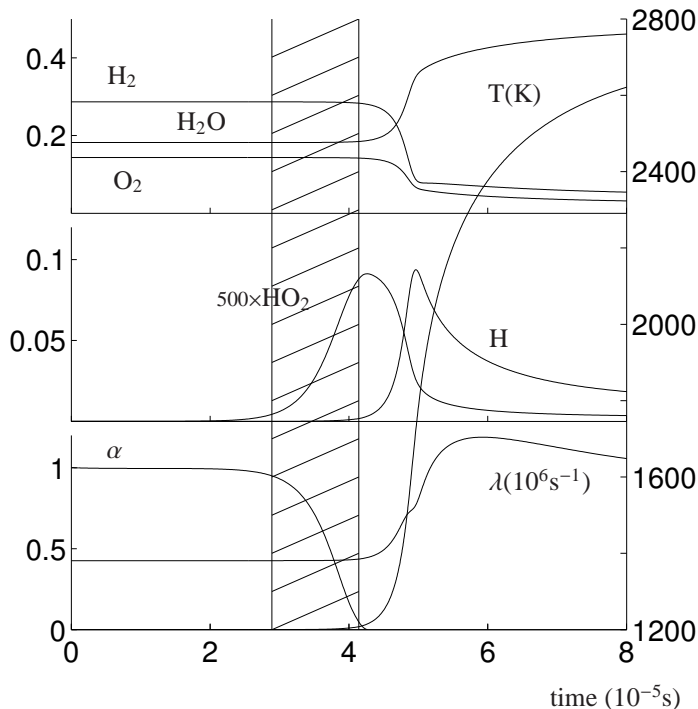
10

Figure 13: Evolution of the mole fractions of the main species (top), of H and HO_2 radicals (middle), reactivity λ and autoignition criteria α (bottom), and temperature (full-height), during isobaric homogeneous autoignition. Vertical lines at α=0.95 and 0.05.

pends very little on the choice α_{min}, provided it is sufficiently small (also described in [9]). However, the value of α_{max} sets the sensibility of the criterion. It has to be small enough to be insensitive to numerical instabilities, but large enough to capture the induction region. Figures in the next section show that $\alpha_{max} = 0.95$ is a good choice.

4.3. Identifying autoignition

The stabilization of a turbulent lifted flame by autoignition is more complex than the homogeneous case described in Fig. 13. However, the discussion stands in reactive preheated turbulent mixtures, and the region where α is between α_{max} and α_{min}, may be identified as the autoignition kernel.

Figure 14 represents on the left the area corresponding to $0.05 < \alpha < 0.95$ in the symmetry plane, and on the right the isosurfaces of α=0.05 and 0.95 colored with the reactivity λ, computed from an instantaneous solution obtained with the reduced chemistry. As a reference, a gray temperature isosurface at T=1600K is also plotted, delimiting the burnt gases region. For visualization purposes the α isosurfaces were restricted here to very reactive mixtures, eliminating points where λ is smaller than one third of its maximum value. The volume corresponding to $0.05 < \alpha < 0.95$, well separated from the burnt gases, can then be associated to the autoignition kernel.

Further study of this ignition kernel shows that it contains pockets of burnt gases, some of these pockets readily visible in Fig. 14. The strict separation of the burnt gases region and

the autoignition kernel in Fig. 14 shows the efficacy of the method as an identifier of autoignition. Upstream, the autoignition kernel shows finger-like shapes, corresponding to the first detectable stages of autoignition. The coloring indicates that autoignition at this first spots occurs at maximum values of λ, that is, at the most reactive mixture, as should be expected.

In addition, this method can be adapted to syngas autoignition (H_2 : CO mixtures). The expression for the reactivity Eq. (5) remains valid, as the chain-branching is dominated by H_2 chemistry. The chemical steady-state parameter for HO_2, α, includes additional CO related reaction rates [32].

It should be remarked that the expression for the reactivity is not valid below the second explosion limit, where autoignition is not controlled by the chain-branching, but by a thermal runaway [33].

5. Conclusions

We have presented simulations that validate a three-step reduced kinetic-chemical mechanism for H_2 oxidation [9] in a turbulent, autoignition-stabilized flame. As outlined in the introduction, one of the main motivations for studying reduced chemistry is the possible saving in computational costs. The use of the reduced chemistry results in a significant 20% speed-up compared to the detailed mechanism. Note that a speed-up of up to 45% was obtained using the reduced mechanism in a two-dimensional cartesian grid DNS solver [26]. Higher speed-up, of up to 75%, was obtained in transported PDF simulations. These differences in speed-up can be related to the different relative weight of chemistry integration in the cost of the three simulation methods.

The reduced mechanism for H_2 oxidation [9] offers an attractive alternative to detailed chemistry as being computationally cheaper, and leading to practically identical results. For it was derived in a fully explicit manner, no tuning is necessary prior to a flame computation and it can be readily adapted to any H_2-oxidation detailed chemistry available in the literature.

The simulation using the reduced chemistry is as stable as the computation with the complete chemistry. The modification of the three global reaction rates where $\alpha > 0.05$ has proven to be an effective correction even in a turbulent simulation, and, more importantly, does not cause any particular numerical instability. Given the excellent results obtained with the reduced chemistry in laminar combustion [9], and its accuracy in this lifted flame, it is expected to give good results in other turbulent lifted flames as well, provided that autoignition occurs at conditions above the 2nd explosion limit.

Based on the quantities introduced in [9], an efficient autoignition detection methodology was presented in the last section. This method is computationally cheap, as all quantities are given by explicit formulas, and can be adapted to any H_2-air oxidation scheme, provided that the hydroperoxyl radical HO_2 is included in the mechanism. This includes also any H_2-dominated autoignition process, for instance that of syngas (H_2 : CO) mixtures. Also, it provides a simple way to evaluate the most-reacting mixture fraction in a mixing-layer. A
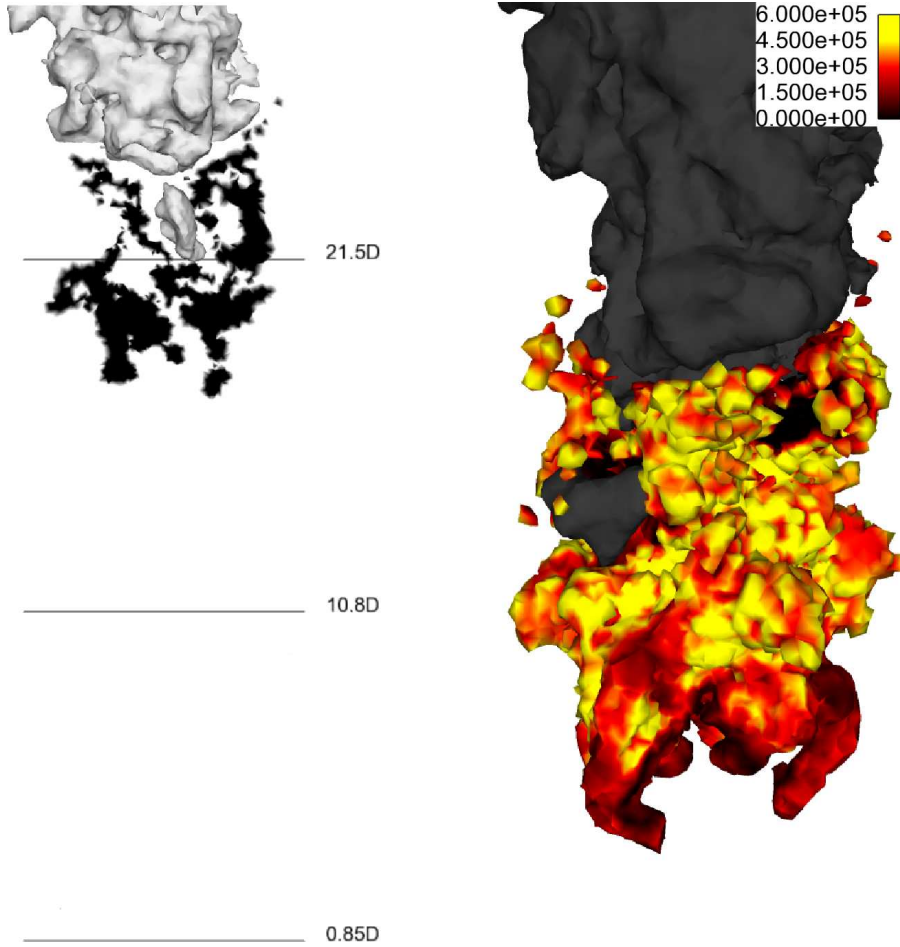
Figure 14: Left: in black, area corresponding to $0.05 < \alpha < 0.95$ in the symmetry plane. Right: zoom on the iso-surfaces $\alpha = 0.05$ and 0.95, colored with λ. In gray, temperature isosurface at T=1600K.

similar method for more complex fuels should be further investigated, starting with a systematic simplification of the autoignition process. The resulting system might not resolve to a simple quadratic expression, as for the hydrogen mixtures reactivity, or even be fully explicit, but it should remain cheaper computationally than analyzing the complete Jacobian of the chemical source term, whose complexity grows with the square of the number of species.

Additionally, this study enlightens the fact that the choice of the chemistry scheme in a simulation of an autoignition-stabilized lifted flame is essential, as an inappropriate choice can lead to errors on the flame stabilization-height of up to 50%.

Appendix A. Resolution in the stabilization region

No subgrid scale turbulent combustion model is used in the present simulations, that are considered DNS in the flame stabilization regions. This was justified a priori in 2.3, as a result of a very fine mesh resolution in the near burner region (from $x = 0$ to $x = 40$ D). This refined region should contain the area of interest for this study, estimated from laminar flame results to cover a region up to x/D=30 for autoignition and a region up to x/D=50 for the stabilization point. It can readily be seen from Figs. 3, 4 and 12, that also in the turbulent flame case, the stabilization region is included in the well resolved area.

Additionally, an a posteriori test for the resolution in this region can be obtained by comparing the SGS turbulent viscosity μ_t and the laminar viscosity μ in this region. Figure A.15 shows an instantaneous plot of the ratio μ_t/μ in the central plane of the simulation, in which contour lines of reactivity λ are superimposed. In the induction region, where mixing and autoignition occur, that is, in the region delimited by the $\lambda = 10^5$ contours, the SGS turbulent viscosity is less than an order of magnitude larger than the laminar viscosity $\mu \approx 5.10^{-5}$ kg/m s. This shows that the turbulent structures in the induction area are well resolved.

Finally, the resolution issue has also been tested when examining the scatter plots in Figs. 7 and 8, for $x/D \leq 40D$. The fluctuations in the mixture fraction space f obtained in the simulation cover a similar range than the mixture fraction measured in the experiment, although some differences are observed. This means that the resolved scales in f represent the experimental fluctuations, and no SGS fluctuation model is needed. Further in the flame, after 40 D, for example in Fig. 9, a first hint of possible subresolution in f appears.
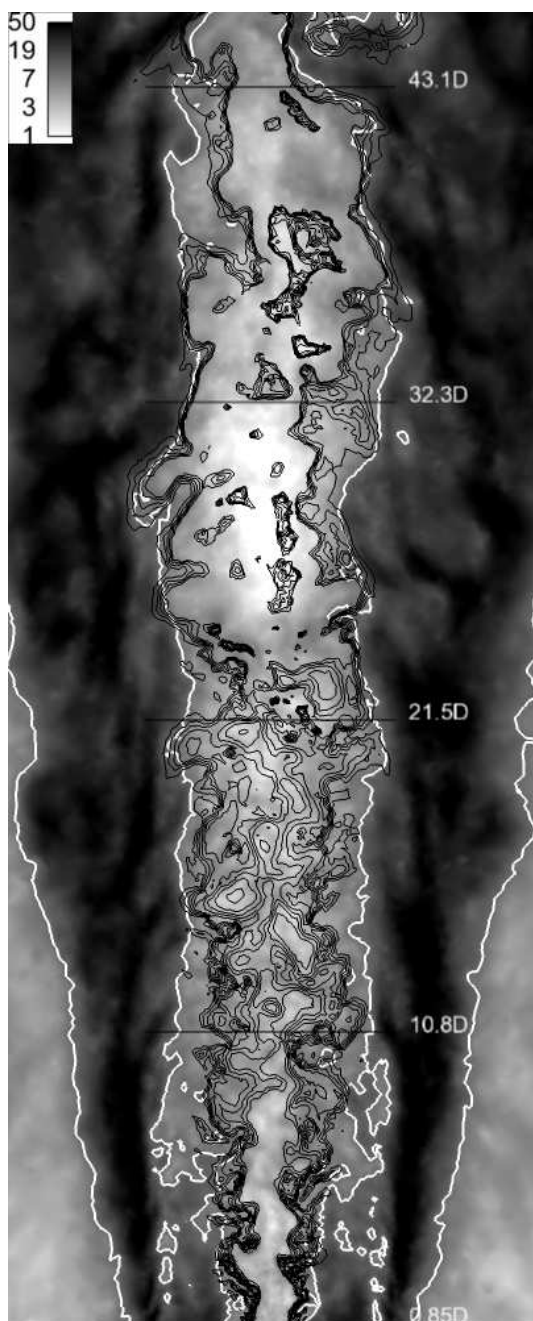

Figure A.15: The ratio μ_{turb}/μ_{lam}, and isocontours of the reactivity $\lambda = k.10^5 s^{-1}$, $k = 1, 2, .., 5$ delimiting the autoignition region. The white line is situated at $\mu_{turb}/\mu_{lam} = 10$.

References

[1] P. Saxena, F.A. Williams, Combust. Flame 145 (2006) 316–323. http://maeweb.ucsd.edu/~combustion/cermech/.

[2] F.A. Williams, J. Loss Prev. Proc. Indust., 21 (2008) 131–135.

[3] F. Mauss, N. Peters, B. Rogg, F. A. Williams, in: Reduced Kinetic Mechanisms for Applications in Combustion Systems, N. Peters, B. Rogg, (Eds.) Springer-Verlag, Heidelberg, 1993, pp. 29–43.

[4] K. Seshadri, N. Peters, F. A. Williams, Combust. Flame 96 (1994) 407–427.

[5] D. Fernández-Galisteo, A.L. Sánchez, A. Liñán, F. A. Williams *Combust. Flame* 156 (2009) 985–996.

[6] D. Fernández-Galisteo, A.L. Sánchez, A. Liñán, F. A. Williams *Combust. Th. Modelling* 13 (4) (2009) 741–761.

[7] E. Guthiel, G. Balakrishnan, F.A. Williams, in: Reduced Kinetic Mechanisms for Applications in Combustion Systems, N. Peters, B. Rogg, (Eds.) Springer-Verlag, Heidelberg, 1993, pp. 177-195.

[8] G. Balakrishnan, M.D. Smooke, F.A. Williams, Combust. Flame,102 (1995) 329–340.

[9] P. Boivin, C. Jiménez, A. L. Sánchez, F.A. Williams, Proc. Combust. Inst. 33 (2010) 517-523.

[10] H. Yamashita, M. Shimada, T. Takeno, Proc. Combust. Inst. 26 (1996) 27-34.

[11] T.F. Lu, C.S. Yoo, J.H. Chen, C.K. Law, J. Fluid Mech. 658 (2010) 45–64

[12] Y. Mizobuchi, S. Tachibana, J. Shinio, S. Ogawa, T. Takeno, Proc. Combust. Inst. 29 (2002) 2009–2015.

[13] E. Mastorakos, Prog. Energy Combust. Sci. 35 (2009) 57–97

[14] T. Echekki, J.H. Chen, Combust. Flame 134 (2003) 169–191

[15] P. Domingo, L. Vervisch, D. Veynante, Combust. Flame 152 (2008) 415–432.

[16] T. S. Cheng, J. A. Wehrmeyer, R. W. Pitz, O. Jarrett, G. B. Northam, Combust. Flame 99 (1994) 157-173.

[17] T. Schönfeld, M. Rudgyard, AIAA Journal 37 (1999), 1378–1385

[18] A. Dauptain, B. Cuenot and L.Y.M. Gicquel, AIAA Journal, 48 (2010), 2325-2338.

[19] A. W. Cook, W. H. Cabot, J. Comput. Phys. 203.2 (2005) 379–385

[20] H. Möbus, P. Gerlinger, D. Brüggemann, Combust. Flame 124 (2001) 519–534.

[21] H. Möbus, P. Gerlinger, D. Brüggemann, Combust. Flame 132 (2003) 3–24.

[22] P. Gerlinger, K. Nold, M. Aigner, Int. J. Numer. Meth. Fluids 62 (2010) 1357–1380.

[23] J.F. Izard, A. Mura, C. R. Mécanique 337 (2009) 362–372.

[24] Z.X. Gao, C.H. Lee, SCIENCE CHINA Technological Sciences 53 (2010) 3379–3388.

[25] R.A. Baurle, S.S. Girimaji, Combust. Flame 134 (2003) 131–148.

[26] R. Knikker, A. Dauptain, B. Cuenot, T. Poinsot, Combust. Sci. Technol. 175 (2003) 1783–1806.

[27] A. Liñán, A. Crespo, Combust. Sci. Tech. 14 (1976) 95–117.

[28] W.P. Jones and S. Navarro-Martinez, Combust. Flame 150 (2007) 170–187.

[29] Z. Luo, C.S. Yoo, E.S. Richardson, J.H. Chen, C.K. Law, T. Lu, Combust. Flame (2011).

[30] S.H. Lam, D.A. Goussis, International Journal of Chemical Kinetics 26 (1994) 461–486.

[31] G. del Alamo, F.A. Williams, A.L. Sánchez, Combust. Sci. Tech. 176 (2004) 1599–1626.

[32] P. Boivin, C. Jiménez, A. L. Sánchez, F.A. Williams, Combust. Flame 158 (2011) 1059–1063.

[33] P. Boivin, A. L. Sánchez, F.A. Williams, Combust. Flame (2011) in press. doi:10.1016/j.combustflame.2011.08.019